



One-step Sb(III) decontamination using a bifunctional photoelectrochemical filter

Mohua Li^a, Yanbiao Liu^{a,b,*}, Chensi Shen^{a,b}, Fang Li^{a,b}, Chong-Chen Wang^c, Manhong Huang^{a,b}, Bo Yang^{a,b}, Zhiwei Wang^{b,d}, Jianmao Yang^e, Wolfgang Sand^{a,f}

^a Textile Pollution Controlling Engineering Center of Ministry of Environmental Protection, College of Environmental Science and Engineering, Donghua University, 2999 North Renmin Road, Shanghai, 201620, China

^b Shanghai Institute of Pollution Control and Ecological Security, 1239 Siping Road, Shanghai, 200092, China

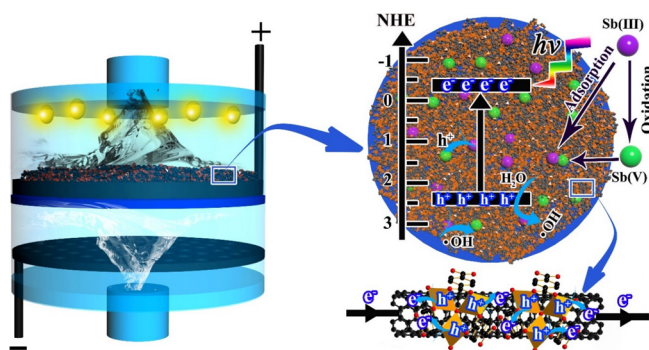
^c Beijing Key Laboratory of Functional Materials for Building Structure and Environment Remediation, Beijing University of Civil Engineering and Architecture, Beijing, 100044, China

^d State Key Laboratory of Pollution Control and Resource Reuse, School of Environmental Science and Engineering, Tongji University, Shanghai, 200092, China

^e Research Center for Analysis & Measurement, Donghua University, 201620, Shanghai, China

^f Institute of Biosciences, Freiberg University of Mining and Technology, Freiberg, 09599, Germany

GRAPHICAL ABSTRACT



ARTICLE INFO

Editor: Danmeng Shuai

Keywords:

Photoelectrochemical
Metal-organic frameworks
Continuous-flow
Oxidation
Sequestration

ABSTRACT

Developing advanced technologies to achieve decontamination of emerging contaminants such as antimony (Sb) is highly demanded. Herein, we successfully designed a dual-functional photoelectrochemical filter system for “one-step” detoxification and sequestration of highly toxic Sb(III). The key to this technology is a photoelectrical-responsive CNT filter functionalized with nanoscale MIL-88B(Fe) photocatalysts. At 2.5 V and under illumination, a $97.7 \pm 1.5\%$ Sb(III) transformation and a $92.9 \pm 2.3\%$ Sb_{total} removal efficiency can be obtained using an optimal hybrid filter (e.g. CM(50:3)) over 2 h continuous filtration. This can be explained by the synergistic effects of the filter’s flow-through design, photoelectrochemical reactivity, fine pore size, and plentiful exposed sorption sites. Various advanced characterization techniques validated the system efficacy. Improved Sb(III) removal kinetics were observed when compared with conventional batch system (97.5% vs 75.8%). A synergistic effect between photocatalytic (PC) and electrochemical (EC) process were identified ($k_{PEC} = 0.99\text{ h}^{-1} > k_{PC} = 0.21\text{ h}^{-1} + k_{EC} = 0.30\text{ h}^{-1}$). EPR and photochemical characterizations suggested that hydroxyl radicals dominated the Sb(III) conversion. The proposed technology works effectively across a wide range of pH

* Corresponding author at: Textile Pollution Controlling Engineering Center of Ministry of Environmental Protection, College of Environmental Science and Engineering, Donghua University, 2999 North Renmin Road, Shanghai, 201620, China.

E-mail address: yanbiaoliu@dhu.edu.cn (Y. Liu).

<https://doi.org/10.1016/j.jhazmat.2019.121840>

Received 4 November 2019; Received in revised form 25 November 2019; Accepted 5 December 2019

Available online 09 December 2019

0304-3894/ © 2019 Elsevier B.V. All rights reserved.

values and water matrixes. The outcomes of this study can facilitate mechanistic insights into photoelectrocatalysis and provide a promising nanotechnology for efficient Sb(III) decontamination.

1. Introduction

The removal of antimony (Sb), an emerging contaminant, from surface waters is becoming highly demanded (Qi et al., 2018; Ungureanu et al., 2015). The most abundant species of Sb are those based on inorganic antimonite (i.e. Sb(III)) and antimonate (i.e. Sb(V)), and Sb(III) is 10 times more toxic than Sb(V) (Filella et al., 2012). Various advanced technologies have been developed to address this challenging issue, e.g. adsorption, membrane filtration, and chemical precipitation (Qi et al., 2019; Zhao et al., 2019; Kong et al., 2015; Guo et al., 2018a). Among these methods, adsorption is evolving as a promising remediation technique for Sb decontamination due to its cost effectiveness and robust operation (Das et al., 2017; Saleh et al., 2017). However, even though negatively charged Sb(V) could be efficiently removed by adsorption, these neutrally charged Sb(III) with higher toxicity may still survive during this removal process. In consequence, a two-step “oxidation-precipitation” strategy is adopted for Sb(III) removal, i.e. to oxidize Sb(III) to less toxic Sb(V) firstly, followed by chemical precipitation treatment (Wu et al., 2019). Unfortunately, there are three practical deficiencies in such two-step approach: (i) increased system complexity and cost, (ii) slow reaction kinetics due to the limited concentration of Sb(III) in water bodies, and (iii) excessive consumption of chemicals (e.g. flocculants/bases for Sb(V) precipitation) (Guo et al., 2018a).

Among these various adsorbents that have been developed and investigated (Zhao et al., 2019; Rangwani et al., 2018; Li et al., 2019), metal-organic framework (MOFs) materials hold considerable promise. MOFs are a class of porous materials composed of metal nodes and organic linkers by coordination binding, well known for their tailorable functionality, high surface area, and tunable channel dimensions (Wang et al., 2014; Trickett et al., 2017). On one hand, recent studies have demonstrated the efficacy of few MOFs materials (e.g. UiO-66, ZIF-8 and Fe-BTC) for the sorption-removal of heavy metal ions (e.g. As and Sb) (Rangwani et al., 2018; He et al., 2017; Jian et al., 2016; Zhu et al., 2012). In particular, the employment of Fe-based MOFs as sorbents have drawn widespread attention due to their cost-effectiveness, earth-abundance, and non-toxic (Lin et al., 2018; Dao et al., 2019). For example, Cai et al. reported that the regular fine pores of MIL-100(Fe) nanoparticles facilitated the transport of arsenate anions towards unsaturated Fe(III) sites (Cai et al., 2016). However, these nanoscale sorbents have rarely been applied to practical processes due to the additional efforts needed for post-separation. In addition, despite a certain progress in adsorption capacity, the knowledge of the sorption kinetics is still far from being complete. Several designs proposed to attach these sorbents onto support materials, encapsulate into polymers, or blend into membranes (Nguyen Tien et al., 2020; Liu et al., 2020; Buruga et al., 2019). Unfortunately, this may still deteriorate the performance by blocking the active sites. Also, it is of note that most of the previous studies only focused on conventional batch reactors where diffusion dominates the mass transport of the target compounds (Antonellini et al., 2017; Majumder et al., 2011). Despite good hydraulic mixing, slow near-surface and internal diffusion can limit the overall kinetics. This leads to only fractional utilization of their sorption capability. Such issue can be partially addressed by adopting an alternative flow-through design with convection-enhanced mass transport (Zhou et al., 2011).

On the other hand, MOFs possess abundant and uniformly active sites (metals or organic links) that are accessible for the guest molecule via opened channels (Du et al., 2019a), which are anticipated to assume a relevant potential as a high-performance photocatalyst towards

detoxification of heavy metals. For example, Du and colleagues reported that an amine-functionalized UiO-66(Zr/Hf) photocatalyst displayed efficient reductive capability for the detoxification of hexavalent chromium (Cr(VI)) to less toxic trivalent chromium (Cr(III)) in a conventional batch system (Du et al., 2019b). However, it still suffers from serious photocarriers recombination issues. As previously reported, the charge recombination rate of electron-hole pairs is 2–3 orders of magnitude faster than that of charge separation and transfer in crystalline photocatalyst, which significantly limited the efficiency and practicality (Guo et al., 2018b; Zhu et al., 2017). This issue could be alleviated by applying a bias potential across the electrodes, i.e. photoelectrocatalysis, which results in the improved separation of photo-generated electron/hole pairs and make better use of photogenerated holes (Dalle et al., 2019; Cong et al., 2017).

Here, we rationally designed a photoelectrochemical filter composed of a Fe-based MOF (e.g. MIL-88B(Fe)) and carbon nanotubes (CNT) for “one-step” Sb(III) decontamination. The objective of this proof-of-concept study is to simultaneously oxidize and adsorb highly toxic Sb(III) using a photoelectrochemical filtration system. In this design, both the MIL-88B(Fe) and the CNT are indispensable. In particular, the photoresponsive MIL-88B(Fe) serves as a high-performance photocatalyst and an adsorbent. Upon illumination of the MIL-88B(Fe), pairs of electron and hole were excited. These photogenerated holes are strong oxidants enabling oxidation of Sb(III) directly or inducing the production of other reactive oxygen species (e.g. hydroxyl radicals) indirectly. The Fe-based MOF could also sequester the as produced Sb(V) due to their high affinity. The CNT serves as conductive scaffolds to support these nanoscale MIL-88B(Fe) and to conduct produced photo-generated electrons. To do this, we firstly developed a facile method to fabricate the photoelectrochemical filter with MIL-88B(Fe) nanoparticles uniformly coated onto the CNT sidewalls. We also modified a commercial filtration casing to introduce electrochemistry and photochemistry into the flow-through system. We hypothesized that: (1) Sb(III) could be effectively oxidized to low toxic Sb(V) within the photoelectrochemical process, (2) the as-obtained Sb(V) could then be effectively sequestered by the loaded MOFs, (3) a flow-through design would accelerate the convection-enhanced mass transport of Sb(III), and (4) the charge recombination rate within the photoelectrochemical system could be greatly inhibited by the applied electric field. To the best of our knowledge, it is the first report describing the integration of MOF and carbon for the simultaneous detoxification and sequestration of heavy metal ions in a flow-through manner. The outcomes of this study provide a promising photoelectrochemical strategy by integrating MOFs photocatalysis and electrochemical CNT filters for Sb decontamination from water bodies.

2. Materials and methods

2.1. Chemicals and materials

All the chemicals used in this work were of analytical grade and without further purification. Dimethylformamide (DMF, $\geq 99.5\%$), sodium sulphate (Na_2SO_4 , $\geq 96\%$), nitric acid (HNO_3 , 36–38%), perfluorinated resin solution (Nafion, 5%) and iron chloride hexahydrate ($\text{FeCl}_3 \cdot 6\text{H}_2\text{O}$) were purchased from Sinopharm Chemical Reagent Co., Ltd. (China). Sb(III) and Sb(V) stock solutions were prepared with potassium antimonyl tartrate trihydrate ($\text{C}_8\text{H}_4\text{K}_2\text{O}_{12}\text{Sb}_2 \cdot 3\text{H}_2\text{O}$) and hydrated potassium antimonate ($\text{KSb}(\text{OH})_6$). 1,4-Benzenedicarboxylic acid (BDC) was purchased from Sigma-Aldrich. Multi-walled CNT ($\langle d \rangle = 10\text{--}20\text{ nm}$ and $\langle l \rangle = 10\text{--}30\text{ }\mu\text{m}$) was provided by TimesNano

Co., Ltd. (Chengdu, China). All the aqueous solutions were prepared with ultrapure water produced from a Milli-Q Direct 8 purification system (Millipore, USA).

2.2. Preparation of O-CNT@MIL-88B(Fe) photoanode filter

Carboxylate CNTs (or O-CNTs) were prepared by refluxing CNT powders in HNO_3 at 70°C for 12 h (Gao and Vecitis, 2011). O-CNTs@MIL-88B(Fe) (or CM) composites were fabricated by a solvothermal route using DMF as reaction medium. In a typical procedure, 15 mg O-CNTs were homogeneously dispersed in 15 mL DMF by ultrasonication, followed by the addition of 0.075 mmol $\text{FeCl}_3 \cdot 6\text{H}_2\text{O}$ to chelate Fe^{3+} onto the O-CNTs surface. Then, 0.075 mmol terephthalic acid (TPA) and 10 mL DMF were added dropwise into the above solution. The mixture was then transferred into a 30 mL Teflon-line autoclave and heated at 150°C for 3 h. After solvothermal reaction, the products were collected by vacuum filtration onto a PTFE support membrane (pore size of $0.45\ \mu\text{m}$) and washed with copious ethanol and ultrapure water. The loading of MIL-88B(Fe) onto O-CNTs can be fine-tuned by adding different amounts of MIL-88B(Fe) precursors. Based on the molar ratio of CNT to MIL-88B(Fe) ($\text{C}_{24}\text{H}_4\text{O}_{13}\text{Fe}_3$, $M = 667.8\ \text{g/mol}$), the composite was denoted as CM(50:1), CM(25:1), CM(50:3), and CM(25:2).

2.3. Characterizations

The crystalline phases of CNT and CM hybrids were characterized using a Rigaku D/max-2550 PC thin-film X-ray diffractometer (XRD, Japan) between 5° and 80° using $\text{Cu K}\alpha$ radiation. A Hitachi S-4800 field emission scanning electron microscope (FESEM, Japan) was used to characterize the surface morphologies of pristine CNT and CM filters. Elemental mapping of CM filter was performed in a JEM-2100 F field emission transmission electron microscope (FETEM, JEOL, Japan). X-ray photoelectron spectroscopy (XPS) analyses were conducted under high vacuum (1×10^{-9} Torr) using a Thermo Fisher Scientific Escalab 250Xi XPS instrument (USA). All the binding energies were calibrated and referenced to the C 1s peak at 284.8 eV. UV–vis diffuse reflectance spectrums were acquired on UV–vis spectrophotometer (Hitachi U-3900) with the barium sulfate as a reference. Photoluminescence (PL) spectra were recorded on fluorescence spectrofluorometer (Horiba Jobin Yvon fluoromax-4) with an excitation wavelength of 320 nm. Fourier transform infrared (FTIR) spectra were recorded on a Nicolet NEXUS670 spectrometer using the KBr pellet method. The produced reactive radical species were quantified by using a Bruker EMXnano Bench-Top electron paramagnetic resonance (EPR) spectrometer (Germany), with DMPO as scavenger agent.

2.4. Photoelectrochemical measurements

Photoelectrochemical characterizations were conducted on an electrochemical workstation (Pgstat302N, Metrohm Autolab) under $100\ \text{mW cm}^{-2}$ simulated solar light illumination. 5 mg of as-synthesized samples were dispersed in a mixture of 10 μL ethanol and 10 μL Nafion, and then coated onto a $1\ \text{cm} \times 1\ \text{cm}$ indium tin oxide (ITO)-coated glass. The three electrodes system composed of an ITO-coated glass as working electrode, a Pt foil as counter electrode, and an Ag/AgCl electrode as reference electrode. A 0.05 M Na_2SO_4 aqueous solution was served as electrolyte. The photoresponse of as-prepared electrodes were recorded in a single-compartment quartz cell under chopped light irradiation (on/off cycles of 100 s) at a constant bias potential of 0.3 V vs. Ag/AgCl. The electrochemical impedance spectroscopy (EIS) was performed within a frequency range of 10 to 10^5 with an AC voltage amplitude of 10 mV and a bias potential of 0.1 V vs. Ag/AgCl. Mott-Schottky plots were taken at a fixed frequency of 500 Hz and 1000 Hz with 1 mV amplitude at various potentials.

2.5. “One-step” photoelectrochemical decontamination of Sb(III)

Two different operational modes, i.e. recirculated filtration and batch were comparatively investigated. The photocatalytic, electrochemical, and photoelectrocatalytic processes were compared as well. To do this, we modified a commercial 47 mm polycarbonate filtration casing (Whatman) to simultaneously introduce photochemistry and electrochemistry. Fig. S1 (Supporting Information) presents the schematic illustration of the photochemical filtration device, which includes (1) LED lamps ($\lambda_{\text{max}} = 450\ \text{nm}$); (2) anodic Ti ring; (3) photoanode filter; (4) perforated Ti cathode. We installed eight NSPU510CS LED lamps (NICHIA, Japan) at the top part of the casing. A hollow Ti ring ($D = 35\ \text{mm}$) served as current collector to contact directly with the photoanode filter. Two holes were drilled in the upper and lower parts of the filtration casing as openings for the cathodic and anodic lead. For recirculated filtration, 100 mL of 1 ppm Sb(III) solution were passed through the photoelectrochemical filtration system using an ISmatec REGLO peristaltic pump, and then recycled. An applied voltage of 0–2.5 V was provided by a DC power supply (DH1766A-1, Beijing, China). The solution pH was adjusted by 1 M of HCl or NaOH. As the flow rate directly correlated with the residence time within the filtration device (Liu et al., 2014), a relative slow flow rate of 0.5 mL/min was selected to ensure full contact of Sb species with the active sites on the filter. For the batch mode, the as-prepared photoanode filter and Ti cathode ($2\ \text{cm} \times 5\ \text{cm}$) were suspended in a quartz reactor consisting of 100 mL of 1 ppm Sb(III) at pH 5.5. Aliquots were sampled to examine the reaction kinetics. The concentration of total Sb (Sb_{total}) and released iron ions was determined using a Thermo Scientific iCAP-Q inductively coupled plasma mass spectrometer (ICP-MS, Thermo Fisher Scientific, MA). The concentration of Sb(III) was determined by an AF-610B atomic fluorescence spectrometer (AFS, Beijing, China).

To investigate the effect of common anions on the Sb(III) removal performance, we added 1–10 mM of sulphate, carbonate, phosphate and chloride to the initial Sb(III) solution before flowing through the photochemical filtration system. Sb(III)-spiked tap water and lake water samples were further used to examine the system efficacy in practical conditions. The stability and reusability of optimized filter was evaluated by performing three continuous running cycles of 100 mL of 500 ppb Sb(III) at pH of 5.5. Exhausted filters were regenerated by applying passing through 100 mL of 5 mM HCl solution.

3. Results and discussion

3.1. Characterizations of photoanode filters

The synthesis process of an O-CNT@MIL-88B(Fe) filter was illustrated in Fig. 1. Due to the presence of abundant surface oxygen-containing functional groups, the as-obtained O-CNT not only facilitated their dispersion in DMF, but also provided sufficient sites for Fe^{3+} chelation. Once Fe^{3+} ions were anchored onto the O-CNTs side-walls, the *in-situ* growth of MIL-88B(Fe) on O-CNTs could be initiated after the addition of ligand linker (e.g. TPA). As illustrated in Fig. 2(a–d), individual MIL-88B(Fe) nanoparticles grew uniformly onto the CNTs surface. When the MIL-88B(Fe) precursor concentration was 0.075 mmol (i.e. CM(50:1), see Fig. 2a), the O-CNTs surface became much rougher compared with pristine CNT (Fig. S2, Supporting Information). By further increasing the precursor concentration to 0.150 mmol (i.e. CM(25:1), see Fig. 2b), an increased particle size (7–16 nm) onto the O-CNTs surface can be observed. While the precursor concentration increased to 0.225 mmol (i.e. CM(50:3), Fig. 2c), these fine MOF nanoparticles were uniformly coated onto O-CNTs and formed an inter-connected 3D network. Further increasing the molar ratio of MIL-88B(Fe) to CNTs leads to an evident increase in the particle size, even burying the conductive scaffolds of O-CNTs (see Fig. 2d). This phenomenon may be due to excessive precursor concentration, that increased the disorder of the composites network. Thus, three different

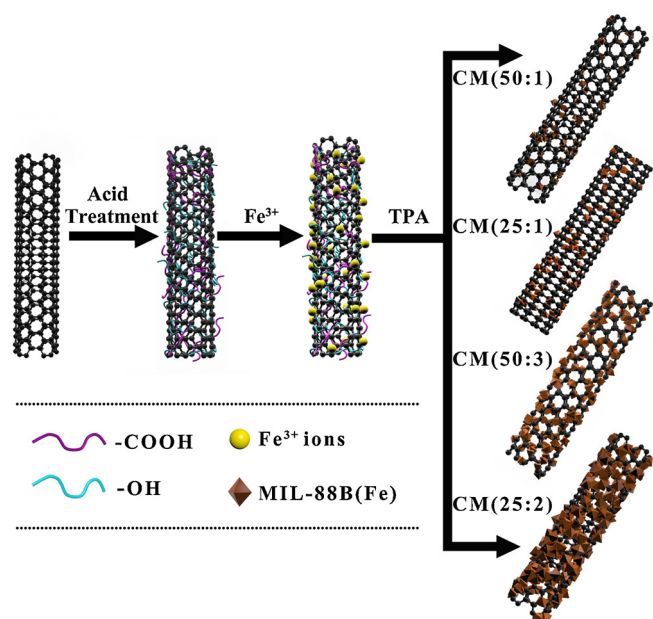


Fig. 1. Schematic illustration of the fabrication route for the CM hybrids.

structure features were identified, *i.e.* loose 3D network (CM(50:1) and CM(25:1)); dense 3D network (CM(50:3)); and irregular agglomerates (CM (25:2)).

Along with the morphological investigation by FESEM, the composition and structure of CNTs, MIL-88B(Fe) and CM composites were further analyzed by powder XRD analysis. As shown in Fig. 2e, the as-prepared MIL-88B(Fe) exhibited a well-defined crystal structure with diffraction peaks in good agreement with those reported for MIL-88B(Fe) by Cambridge Crystallographic Data Centre (CCDC) #647646, confirming the successful fabrication of MIL-88B(Fe) (Horcajada et al., 2011). The dominant diffraction peaks centered at 9.1° , 9.6° , and 10.6° can be assigned to (002), (100), and (101) planes, respectively (Lei et al., 2018). When coated onto the O-CNTs, no evident changes of these characteristic peaks were observed, and no other impurities peaks appeared in the XRD pattern as well. Fig. 2f displayed the structure of MIL-88B(Fe) viewed along the *a* and *c* axis with positions of Fe, O, C elements in a 3D structure. These evidences suggest that we have successfully fabricated the CM composites with MIL-88B(Fe) particles *in situ* grown onto the O-CNTs sidewalls.

The optical absorption spectra of these as-fabricated hybrid filters were recorded by UV-vis diffuse reflectance spectra (DRS). As presented in Fig. 3a, the pure MIL-88B(Fe) only demonstrated absorption within the range of 200–600 nm. The characteristic peak centered at 224 nm can be ascribed to the ligand-to-metal charge transfer (LMCT), and the spin-allowed *d-d* transition at 300–500 nm can be attributed to the presence of Fe^{3+} (Yu et al., 2019). All the hybrid filters demonstrated similar light response curves as pure MIL-88B(Fe), but with an evident red shift. In addition, the presence of O-CNTs resulted in a continuous absorption band in the range of 450–800 nm, which agreed with the black color of the samples (Fig. S3, Supporting Information). Besides, the steady-state photoluminescence (PL) spectra of MIL-88B(Fe) and different hybrid filters were acquired to better understand the separation mechanism of photogenerated charge carriers. As shown in Fig. 3b, at an excitation wavelength of 320 nm, the bare MIL-88B(Fe) displayed emission peaks at ~ 450 nm. After combining with O-CNTs, similar emission peaks can still be observed but with an obviously decreased intensity for these CM hybrids. This indicated that the presence of O-CNTs inhibited the recombination of photo-excited electron-hole pairs, so that more photogenerated electrons and holes can participate into redox reactions (Xu et al., 2019). Furthermore, these O-CNTs also acted as conductive pathways for the rapid transport of photogenerated

electrons through external circuit and further facilitated the highly efficient separation of charge carriers.

3.2. Photoelectrochemical properties of photoanode filters

According to the above analysis, we believed that the as-fabricated CM hybrids may serve as promising high-performance photoanode materials enabling a flow-through design. We, thus, choose the Sb(III) oxidation reaction as a model reaction to evaluate their photochemical activity. We hypothesized that the highly toxic Sb(III) can be transformed to less toxic Sb(V) by passing through the proposed photoelectrochemical system due to the production of reactive species under illumination. As displayed in Fig. 4a, the pure O-CNT alone filter demonstrated a Sb(III) conversion efficiency of $55.1 \pm 3.2\%$ under photoelectrochemical recirculated filtration (at 2.5 V and 0.5 mL/min flow rate), however, with a rather limited Sb_{total} removal efficiency of only $12.7 \pm 2.0\%$. When the surface of O-CNT was loaded with MIL-88B(Fe) nanoparticle, the Sb_{total} removal rate improved significantly, and the best performance was obtained when using CM(50:3) with a $97.7 \pm 1.5\%$ Sb(III) conversion as well as a $92.9 \pm 2.3\%$ Sb_{total} removal within the same period. This can be explained as MIL-88B(Fe) possesses regular fine pores and plentiful active sites, endowing the CM hybrids filters high surface area and high concentration of photo-generated carriers, beneficial for photoelectrochemical applications. Also, due to the high affinity of Sb species to Fe sites, these Sb compounds tend to be effectively sequestered by the loaded MIL-88B(Fe) (Guo et al., 2014; Kong and He, 2016). The enhancement in Sb(III) removal rate when switching from CM(50:1) to CM(50:3) (*i.e.* from loose 3D porous to densely covered 3D network structure) can be ascribed to the increased active sites for photocatalysis and sorption by increasing the loading of MIL-88B(Fe). Nevertheless, further increasing the MIL-88B(Fe) content negatively contributed to the Sb(III) removal performance (*e.g.* from CM(50:3) to CM(25:2)), possibly due to the over-loading of MIL-88B(Fe) that hindered certain conductive CNT scaffolds so deteriorating the charge separation performance. Moreover, the agglomeration of MIL-88B(Fe) particles is inevitable once over-loaded, which led to the reduction of exposed active sites.

To better clarify the improved performance of CM(50:3) towards Sb(III) removal (compared with the O-CNT filter), the change of Sb species with time was compared as summarized in Fig. 4b. When using CM(50:3) photoanode, Sb(III) reached an effluent concentration of 23 ± 10 ppb after 2 h recirculated filtration. In addition, the initial increase in Sb(V) concentration witnessed the continuous Sb(III) oxidation during the photoelectrochemical filtration. Then, Sb(V) became the dominant Sb species, which was further sequestered by the loaded CM(50:3) filter. In contrast, the effluent concentration of Sb(III) only reduced from 1000 ppb to 445 ± 20 ppb by using the O-CNT as anode after 4 h of operation, and the formed Sb(V) increased linearly with time resulting in a limited Sb_{total} removal efficiency of $12.5 \pm 0.6\%$. These results indicated that an O-CNT filter only demonstrated limited oxidation capability of Sb(III), while the anchored MIL-88B(Fe) played two indispensable roles (*i.e.* photocatalyst and adsorbent) during the Sb(III) removal. Firstly, under illumination, nanoscale MIL-88B(Fe) enabled the production of photogenerated holes and electrons. The photogenerated holes and applied electric field synergistically contributed to the rapid Sb(III) detoxification. Secondly, the loaded MIL-88B(Fe) nanoparticles could sequester the Sb species due to their high affinity. As shown in Fig. 4c, the O-CNT filter only demonstrated the capability of Sb(III) oxidation, but failed to sequester these Sb species. While the CM(50:3) filter benefitted from the efficient charge transport from the built-in O-CNTs, which acted as a bridge for photogenerated electrons transfer from MIL-88B(Fe) to external circuit, during photoelectrochemical filtration, enabling the simultaneous Sb(III) oxidation and Sb(V) sequestration.

Detailed morphological and compositional information of the as-prepared CM(50:3) was further obtained by FETEM and EDS mapping

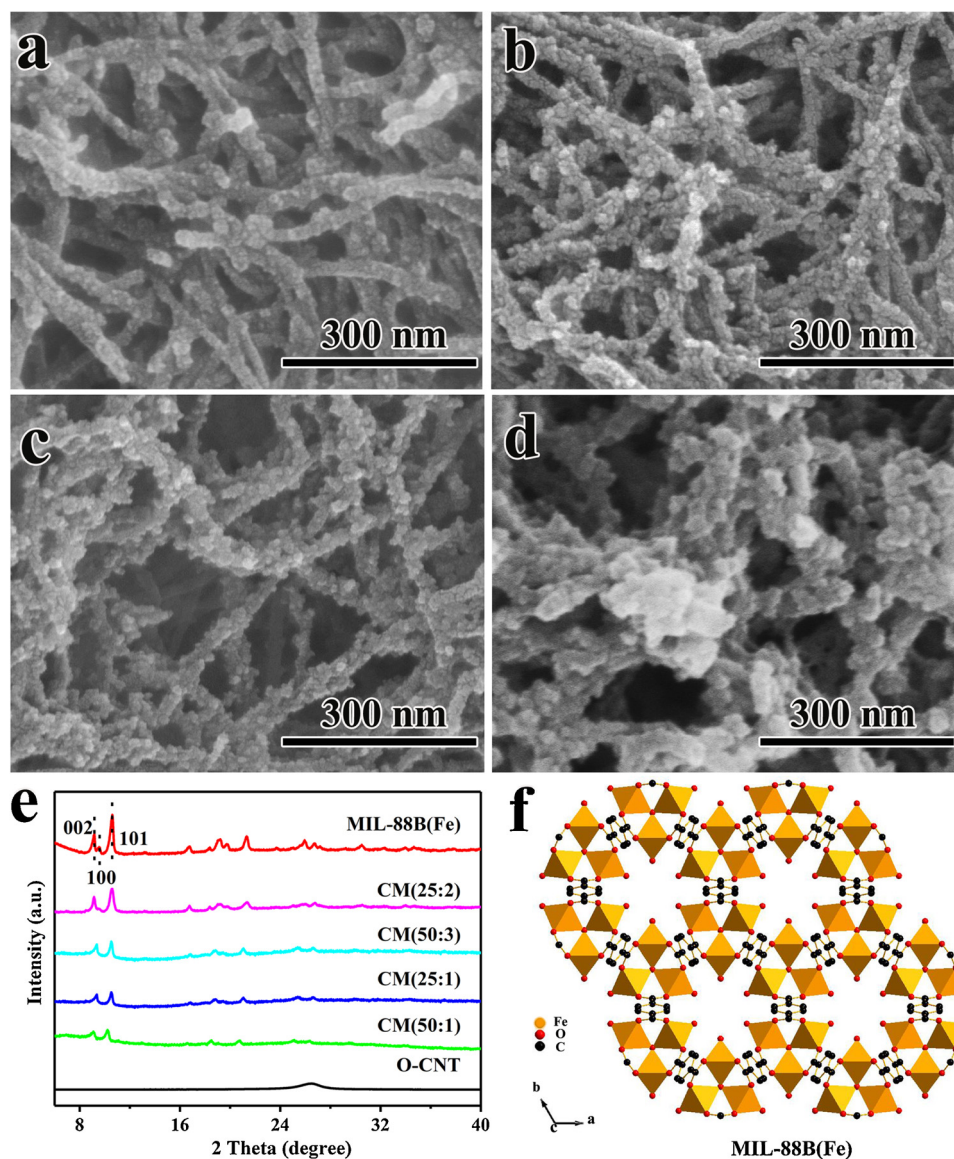


Fig. 2. (a–d) SEM images of as-prepared samples: CM(50:1), CM(25:1), CM(50:3), CM(25:2) composites, respectively. (e) XRD patterns of MIL-88B (Fe), O-CNTs, and their complex products. (f) MIL-88B (Fe) structure viewed along c-axis.

techniques. As shown in Fig. 5a and b, the TEM images of pure O-CNT and CM(50:3) suggested that MIL-88B(Fe) nanoparticles were controllably grafted along the O-CNT sidewall with typical size of 10–20 nm. Additionally, the elemental distribution of CM(50:3) suggests that C, O and Fe were homogeneously distributed over the whole

hybrid (Fig. 5c) with Fe and O elements mainly dispersed at the external surface of the O-CNTs. Furthermore, Fourier transform infrared spectroscopy (FTIR) spectra of CM(50:3) (as shown in Fig. 5d, green curve) also exhibited the vibrations typical of the carboxyl group (at 1600 cm^{-1} and 1390 cm^{-1}), the C–H bending vibration of aromatic

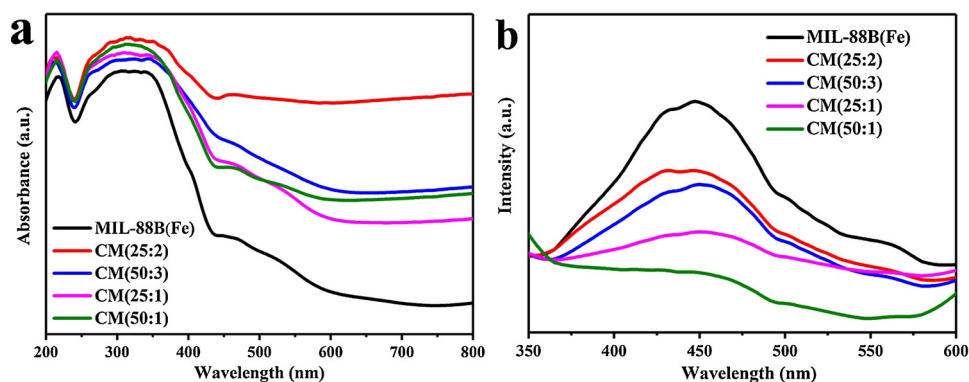


Fig. 3. (a) UV-vis absorption spectra of pure MIL-88B(Fe) and their hybrids. (b) PL spectra of MIL-88B(Fe) and various CM composite materials.

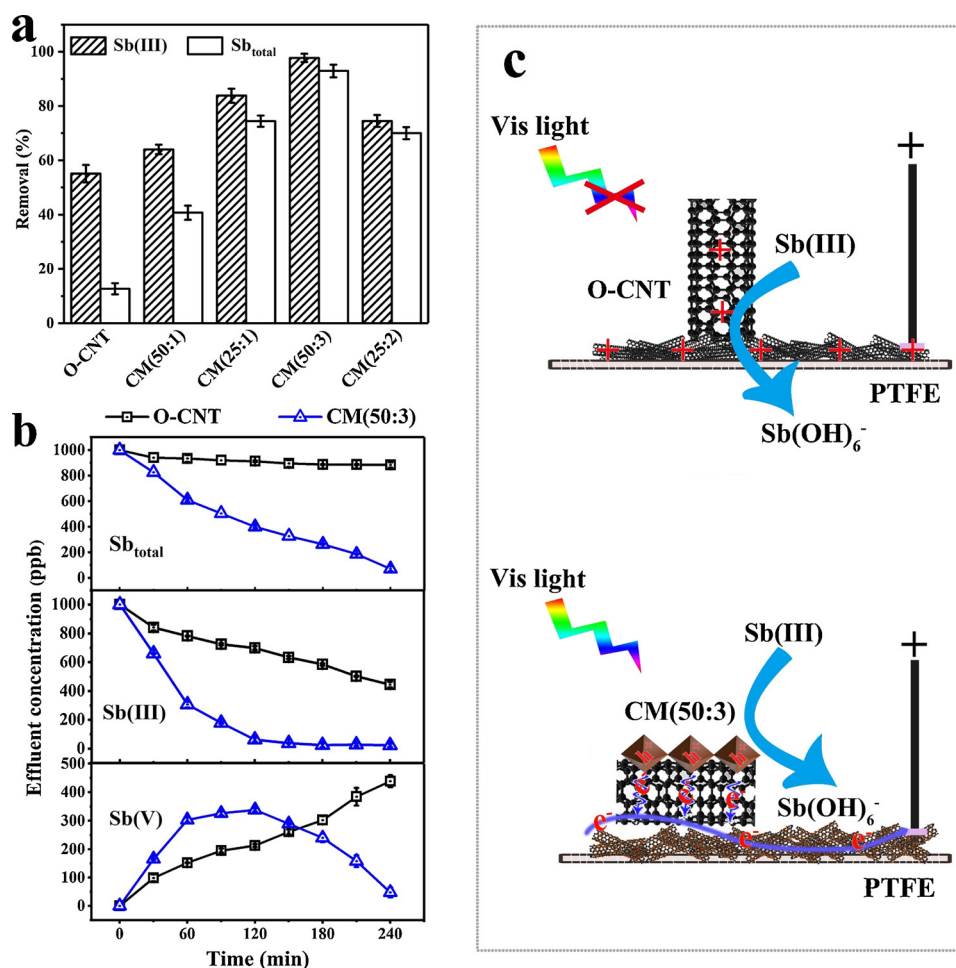


Fig. 4. (a) Sb removal rates of various CM hybrids and O-CNT photoanodes. (b) Changes in Sb species and their concentration as a function of time and different photoanode materials in a typical photoelectrocatalytic system in the recirculation filtration mode. Experimental conditions: [Sb(III)]₀ of 1 ppm, applied voltage of 2.5 V, pH value of 5.5, flow rate of 0.5 mL/min, pH value of 5.5 and 5 mM Na₂SO₄ electrolyte. Error bars reflect standard deviation determined by 5 times experiments. (c) Schematic illustration of the working principle for Sb(III) removal using O-CNT filter and CM hybrid filter.

ring (750 cm^{-1}), and the characteristic peak of Fe-O vibration (at $\sim 540\text{ cm}^{-1}$) (Xie et al., 2017). These agreed well with those typical of pure MIL-88B(Fe). Moreover, the FTIR spectra of O-CNT also proved the successful introduction of oxygen-containing functional groups (e.g. carboxyl: 1600 cm^{-1} and 1390 cm^{-1} , and hydroxyl: 3400 cm^{-1}) after HNO₃ treatment (Duan et al., 2019). This was crucial for the MIL-88B(Fe) heterogeneous nucleation and loading onto the CNTs surface.

To demonstrate Sb(III) conversion and unveil the underlying mechanism using the photoelectrochemical filter, a control experiment in the absence of photo illumination and electric field (*i.e.* sorption only) was conducted (Fig. 6a). The absorption equilibrium of CM(50:3) towards Sb(III) achieved after 2.5 h recirculated filtration, produced an effluent concentration of 626 ± 14 ppb. The corresponding Sb(III) equilibrium adsorption amount (q_e) of CM(50:3) was 5.28 mg/g under sorption-only mode. Similar downward trend was also observed for the change of Sb_{total} effluent concentration, but at a slightly higher value (45 ± 15 ppb), indicating the production of a certain amount of Sb(V) during the adsorption process, possibly originating from the oxidation of coordinately unsaturated iron sites within MIL-88B(Fe) (McKinlay et al., 2013). In contrast, under photoelectrochemical filtration, the Sb(III) effluent concentration exponentially decreased and almost completely vanished within 2 h (Fig. 6b). The Sb(V) became the dominant species, suggesting an evidently accelerated Sb(III) oxidation process under photoelectrochemical filtration. The Sb(III) oxidation rate was much faster than the Sb(V) removal rate within the first 2 h. The maximum Sb(V) concentration was 344 ± 14 ppb at 2 h, and almost

linearly decreased in the following 2 h. This suggested the dominate process within the last 2 h was Sb(V) adsorption. This equivalents to a q_e of 13.1 mg/g under the photoelectrochemical filtration, which was 2.5 times higher than that of the sorption-only process. Two possible reasons could explain this phenomenon: (1) The point of zero charge (PZC) of CM(50:3) filter was determined to be 7.4 (Fig. S4, Supporting Information), thus the filter surface became positively charged at pH 5.5, leading to an electrostatic attraction to these negatively-charged Sb(V). (2) The electric field accelerated both the Sb(III) oxidation kinetics as well as the Sb_{total} removal process (Fig. S5, Supporting Information).

To further unveil the Sb(III) removal pathway, the chemical composition of Sb-loaded CM(50:3) filter after adsorption and photoelectrochemical filtration was examined by XPS technique (see Fig. 6c and d). In the adsorption-alone mode, the Sb 3d + O 1s spectrum can be fitted by four peaks: 530.0 eV, 531.5 eV, 532.2 eV, and 539.4 eV, that corresponds to O_{latt} (lattice oxygen), Sb 3d_{5/2} (Sb(V)), O_{ad} (chemisorbed oxygen species), and Sb 3d_{3/2} (*i.e.* Sb(III)) (Liu et al., 2019; Li et al., 2017). The co-existence of Sb(III) and Sb(V) on the CM(50:3) surface after sorption-only process indicates the occurrence of a slow conversion process of Sb(III) to Sb(V). Contrarily, the characteristic peak of Sb(V) (531.5 eV) sharply increased under photoelectrochemical filtration. The peak centered at 539.4 eV (Sb(III)) shifted to 540.0 eV (Sb(V)), indicating an evidently increased Sb(V) concentration in this case (Wu et al., 2019).

Beyond that, the normalized Sb K-edge XANES spectra (refer to Fig. 6e and f) also provided solid evidence on Sb(III) oxidation.

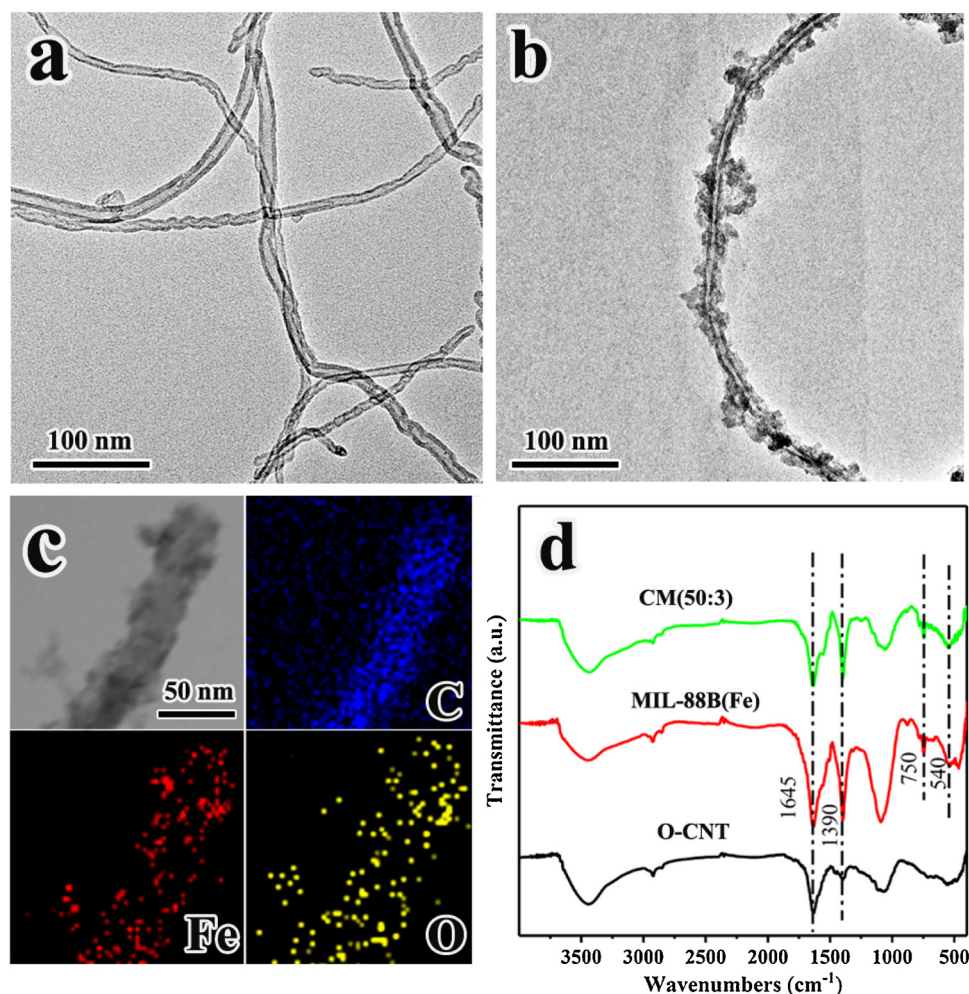


Fig. 5. FETEM images of (a) O-CNTs, (b) CM(50:3) photoanode composite, (c) EDS elemental mapping corresponding to (b) of C, Fe and O, (d) FTIR spectra of O-CNT, MIL-88B(Fe), and CM(50:3) hybrid.

Comparing with the Sb K-edge XANES spectra of pure Sb reference compounds (KSb(OH)_6 and $\text{C}_8\text{H}_4\text{K}_2\text{O}_{12}\text{Sb}_2$ were utilized as reference compounds for Sb(V) and Sb(III), respectively), the mainly oxidation state of Sb on CM(50:3) photoanode filter was Sb(V), consisting with XPS and the AFS results. To gain insights into the sorption mode of Sb on the CM(50:3) filter, FT-IR measurements were conducted to investigate the variation of surface functional groups before and after photoelectrocatalysis of Sb(III) (Fig. S6, Supporting Information). The predominant species for Sb(III) and Sb(V) were Sb(OH)_3 and Sb(OH)_6^- under the experimental pH of 5.5. After photoelectrocatalysis for removal of Sb(III), the absorbance of functional groups (peaks around 1645 cm^{-1} , 1390 cm^{-1} , 750 cm^{-1} , respectively) losing was observed except for O–H bonds (surface adsorbed water, about $3400\text{--}3700\text{ cm}^{-1}$), suggesting that adsorption occurs *via* an inner sphere surface interaction with the formation of Fe–O–Sb bonds (McComb et al., 2007). Moreover, the Fe–O bond shifted to a lower frequency from 540 to 515 cm^{-1} and became less intense, which can be attributed to the strong coordination between Fe and Sb species (Qi et al., 2019). Besides, an emerging characteristic peak was observed in the region below 600 cm^{-1} , where the vibration of Sb–O has been reported (Jana et al., 2016). These findings indicated that chemical adsorption was primarily responsible for the uptake of Sb species.

The synergistic effect of photochemistry and electrochemistry was further studied under different applied potentials using the CM(50:3) filter as an example (see Fig. 7a). The Sb(III) removal efficiency in the adsorption-only process was $38.7 \pm 2.0\%$. While in the presence of

visible light, the photocatalytic Sb(III) oxidation efficiency increased to $54.8 \pm 1.8\%$, indicating an improved Sb(III) conversion kinetics originated from the photocatalytic activity of CM(50:3). The removal rate of Sb(III) further increased with the applied voltage up to 1.5 V (with a $96.0 \pm 3.0\%$ Sb(III) removal efficiency). Further increasing the applied voltage to 2.5 V did not improve the removal performance of Sb(III). This may be due to some competitive oxidation reactions occurring at higher potentials (e.g. water oxidation reaction). Fig. 7b revealed the dynamic trends of Sb(III) (1 ppm) elimination by CM(50:3) filter under different circumstances. In particular, by assuming a classical first-order kinetic law, Fig. 7b reported $\ln(C/C_0)$, where C and C_0 were, respectively, the Sb(III) concentrations at time t and at the beginning of the process, *vs.* t . Straight lines on this plot make it possible to obtain the apparent kinetic constant (k) of the process, k (*i.e.* the absolute value of the line slope). The rate constant under photoelectrochemical condition ($k_{\text{PEC}} = 0.99\text{ h}^{-1}$), was higher than that of electrochemistry process ($k_{\text{EC}} = 0.30\text{ h}^{-1}$), photochemistry process ($k_{\text{PC}} = 0.21\text{ h}^{-1}$) and the sum of them. Subsequently, the synergistic effect of photochemical and electrochemical on the removal of Sb(III) was further studied by synergy index according to previous reports (Zhang et al., 2019). The synergy index (*i.e.* $(k_{\text{PEC}} - k_{\text{PC}} - k_{\text{EC}})/k_{\text{PEC}}$), was calculated to be 0.60, indicating a pronounced synergistic effect between electrochemistry and photocatalysis. This effect can be ascribed to highly efficient electron-hole separation performance as well as inhibited charge recombination within the photoelectrochemical process, and to the unique physicochemical properties of the as-designed anodic filter

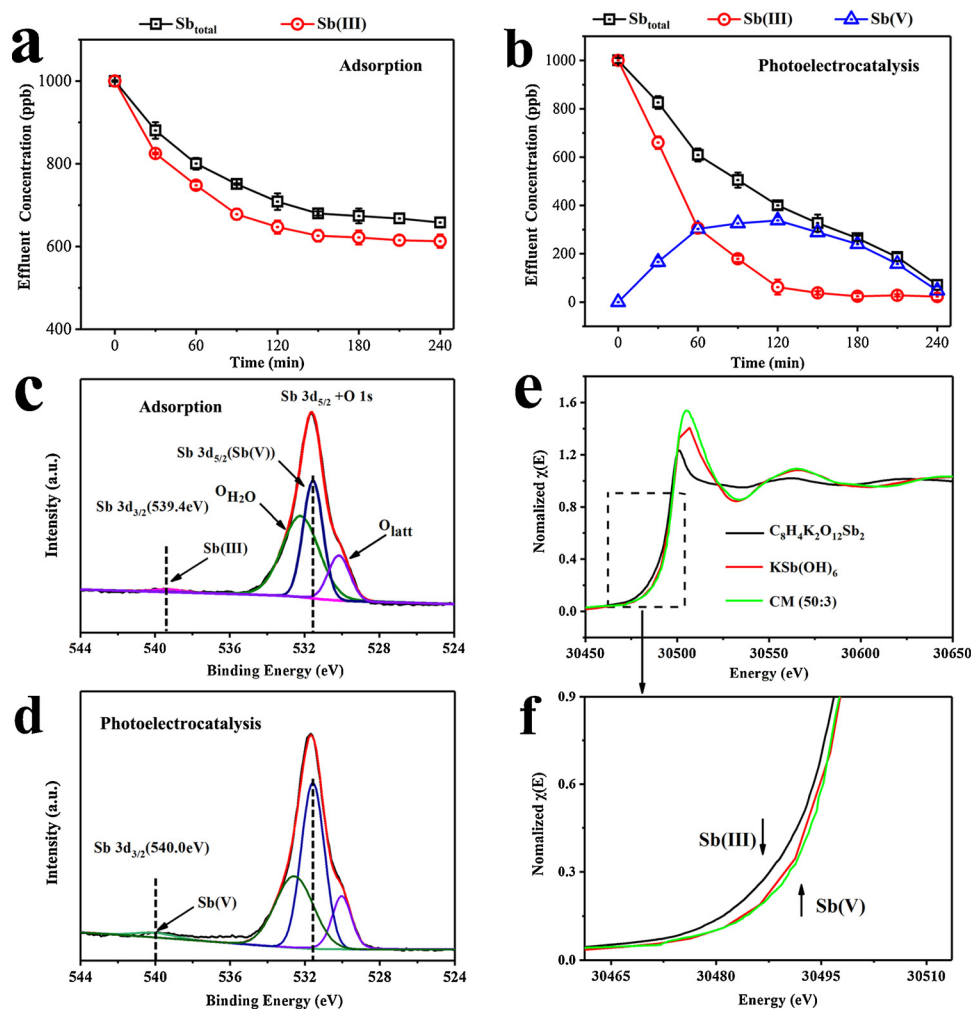


Fig. 6. (a, b) Change of Sb(III) and Sb_{total} concentration in sorption-only and photoelectrochemical filtration using the CM(50:3) filter. Experimental conditions: [Sb(III)]₀ of 1 ppm, applied voltage of 2.5 V, flow rate of 0.5 mL/min, pH value of 5.5, and 5 mM Na₂SO₄ electrolyte. Error bars reflect standard deviation determined by 5 times experiments. (c, d) XPS Sb 3d + O 1s spectra of the Sb-loaded CM(50:3) filter in sorption-only mode and photoelectrochemical filtration mode. (e, f) Normalised Sb K-edge XANES spectra of Sb species adsorbed on the CM(50:3) filter anode.

materials.

Moreover, the Sb(III) removal performance by the photoelectrochemical filter was also comparatively studied with that in a conventional batch system, to gain insight into the operational advantage of a flow-through design (Fig. S7, Supporting Information). The effluent Sb(III) and Sb_{total} concentration over 4 h of recirculated filtration was only 23 ± 10 ppb and 116 ± 15 ppb, respectively. However, the Sb(III) and Sb_{total} concentration in the batch mode was as high as 242 ± 17 ppb and 486 ± 28 ppb, respectively, with the same period

under similar conditions. Such sharp difference suggested an unique advantage of the flow-through design, which significantly enhances the mass transport of Sb(III) and the oxidation product Sb(V) to the active sites of the photoanode filter. Another benefit of the flow-through design is free of sorbents/catalysts recovery. For example, Zhou et al. previously developed an Ag/TiO₂-based continuous-flow photocatalytic reactor with Ag/TiO₂ nanobelts photocatalyst loaded onto a sub-microporous filter paper (Zhou et al., 2011). The photocatalytic degradation performance towards selected model pollutants was

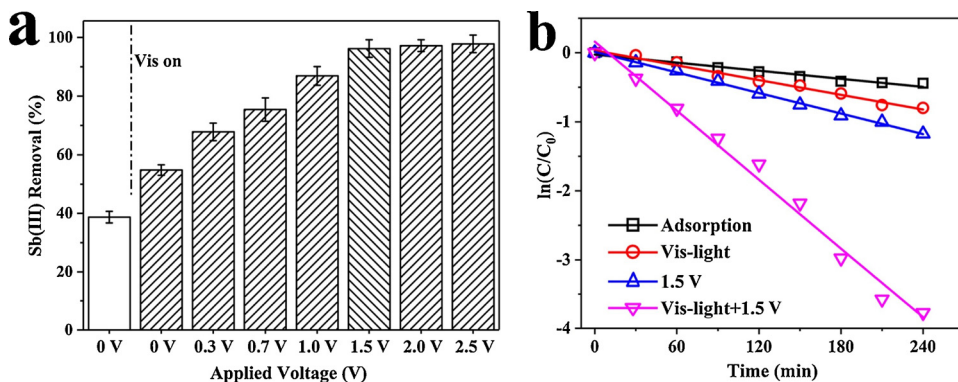


Fig. 7. (a) Sb(III) removal using the CM(50:3) filter as a function of applied voltages (0–2.5 V) under light irradiation. Experimental conditions: [Sb(III)]₀ of 1 ppm, flow rate of 0.5 mL/min, and 5 mM Na₂SO₄ electrolyte. Error bars reflect standard deviation determined by 5 times experiments. (b) Dependence of ln(C/C₀) on irradiation time of CM(50:3) photoanode under different reaction conditions.

improved by the introduction of noble metal cocatalyst (Ag) due to partially inhibited charge recombination rate. However, the high cost related with the usage of noble metal have limited its wide application in environmental field. Alternatively, the proposed photoelectrochemical filter served as an effective and affordable solution. The generated electron/hole pairs from MIL-88B(Fe) could be effectively separated and transferred upon application of a limited electric field. Compared with a previously reported electroactive-only filter (Liu et al., 2019), the integration of photocatalysis, electrochemistry, and membrane separation in the photoelectrochemical filter system allowed for rapid and efficient water treatment, with expected immediate impact and applicability in the treatment of other refractory compounds as well as similar toxic heavy metal ions.

To further explore the function of O-CNTs and MIL-88B(Fe), other physicochemical and photoelectronic characterizations were performed. As displayed in Fig. S8 (Supporting Information), the specific surface area of O-CNT is $147.4 \text{ m}^2 \text{ g}^{-1}$ lower than that of CM(50:3) ($382.3 \text{ m}^2 \text{ g}^{-1}$), and the sample was mesoporous with pores mainly distributed in the range of 3–8 nm. The relatively high specific area of CM(50:3) can be attributed to the introduction of MIL-88B(Fe) and the formation of a densely covered 3D network. In addition, Fig. 8a compared the transient photocurrent responses of MIL-88B(Fe), O-CNT, and CM(50:3) under intermittent visible light illumination. Results indicated that MIL-88B(Fe), O-CNT and CM(50:3) composite all revealed

steady photocurrent responses once the light irradiation was activated. The photocurrent density of CM(50:3) was 1.63 times higher than that of pure MIL-88B(Fe), implying that with presence of O-CNT improved the charge separation performance of photoinduced electron-hole pairs and extended the lifetime of the charge carriers. EIS measurements were also conducted to investigate the interfacial electron transfer of O-CNT, MIL-88B(Fe), and CM(50:3) materials. As displayed in Fig. 8b, where R_{ohm} , R_{ct} , CPE, and W correspond to the electrolyte resistance, transfer resistance, double layer capacitive and diffusion resistance, respectively. Fitting results suggested that the R_{ct} value was 41Ω , 1400Ω , and 471Ω for O-CNT, MIL-88B(Fe) and CM(50:3), respectively. Whereas the R_{ct} of the CM(50:3) nanocomposite was markedly lower than that of the MIL-88B(Fe). This indicated that the CM(50:3) nanocomposite exhibited a decreased electron-transfer resistance. Therefore, within the 3D CM(50:3) composite, the MIL-88B(Fe) component provided a large specific surface area, beneficial for the exposure of Fe-O cluster active sites and the mass transport of target compounds. Moreover, the introduction of CNTs improved the electronic conductivity and facilitates the separation and transfer of photogenerated charge carriers, thus leaving more photogenerated holes participating in the oxidation reaction on the electrode surface.

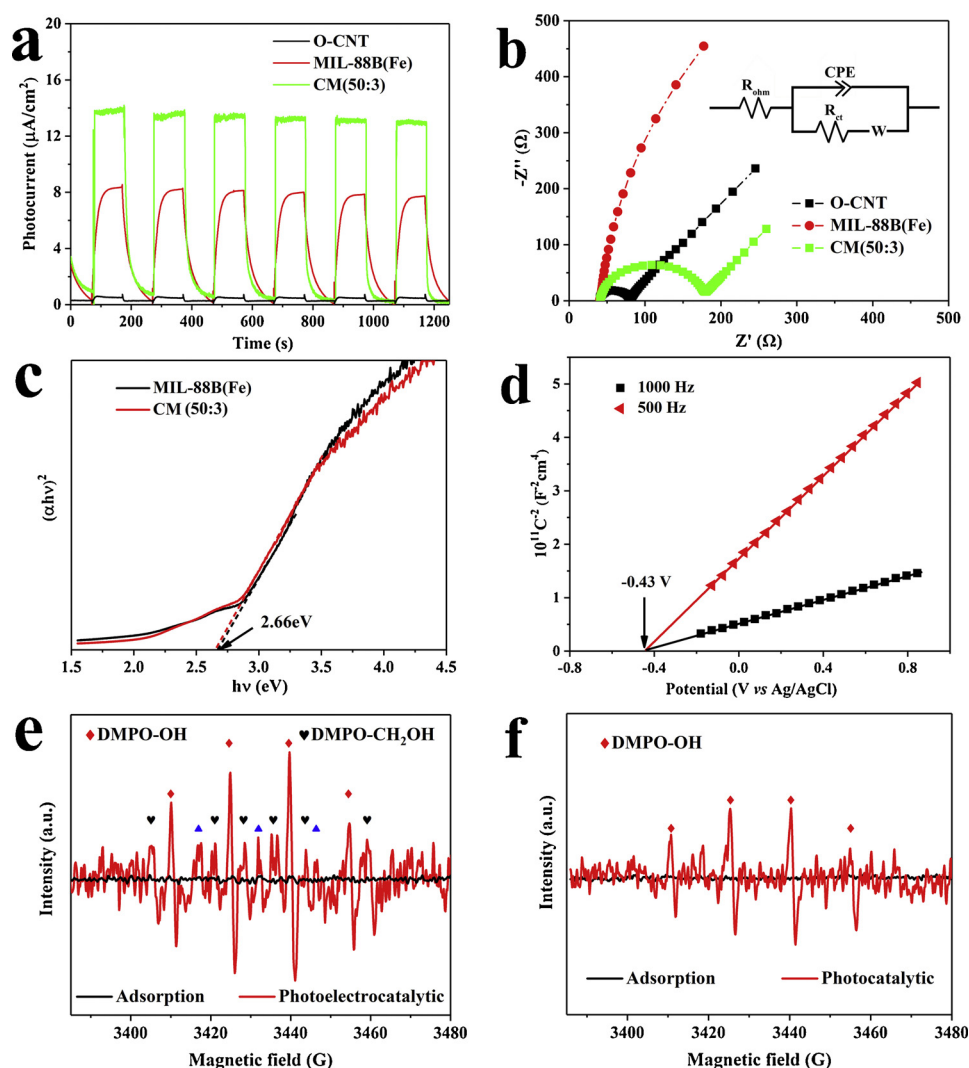


Fig. 8. (a) Transient photocurrent responses, (b) EIS spectra, of O-CNT, MIL-88B(Fe) and CM(50:3). (c) Tauc plots of pure MIL-88B(Fe) and CM(50:3). (d) Mott-Schottky plots of CM(50:3). (e, f) DMPO spin-trapping EPR spectra recorded with CM(50:3) photoanode under different operating conditions.

3.3. Plausible photoelectrochemical working mechanism

To further analyze the working principle of the photoelectrochemical flow-through system, the band structure of the CM(50:3) photoanode filters was taken into consideration. Plots of the transformed Kubelka–Munk function of MIL-88B(Fe) and CM(50:3) were compared to estimate their corresponding band gaps. As shown in Fig. 8c, both MIL-88B(Fe) and CM(50:3) shared a similar band gap of ~ 2.66 eV, implying that the incorporation of O-CNTs in MIL-88B(Fe) did not affect their band structures. Mott–Schottky measurement was applied to determine the flat-band potential (E_{fb}) of CM(50:3) (Fig. 8d). The positive slope indicated that CM(50:3) appears as a n-type semiconductor. It has been reported that the conduction band minimum (CBM) of a n-type semiconductor is closed to its flat-band (Lin et al., 2018), which was calculated to be -0.43 V (vs Ag/AgCl), and the corresponding E_{NHE} value was -0.23 V (vs NHE). This means that the conduction band (E_{CB}) edge was -0.23 V (vs NHE) for CM(50:3). This value was more positive than the potential of $O_2/\cdot O_2^-$ (-0.33 V vs NHE) (Lei et al., 2018). Therefore, the photogenerated electrons could not reduce oxygen and engender $\cdot O_2^-$. Combining the optical band gap and the CBM data together, the valence band (E_{VB}) of CM(50:3) was ~ 2.43 V (vs NHE). In contrast to the oxidation potential of Sb(V/III) ($+0.69$ V vs NHE) and $\cdot OH/OH^-$ ($+2.38$ V vs NHE), the transformation of Sb(III) to Sb(V) using CM(50:3) could be thermodynamically favorable.

EPR technique was employed to identify the responsible reactive species in the proposed photoelectrochemical filtration system. As shown in Fig. 8e and f, signals of DMPO-OH and DMPO-CH₂OH adducts were detected under illumination based on their hyperfine splitting constants (DMPO-OH: $A_N = 14.8$, $A_H = 14.8$; DMPO-CH₂OH: $A_N = 15.5$, $A_H = 22.7$) (Buettner, 1987). Noticeably, the DMPO-OH signal in the photoelectrochemical process was much stronger than that in the photocatalytic process, due to the inhibited charge recombination rate by the applied electric field. Besides, the presence of DMPO-CH₂OH in photoelectrocatalytic process may be due to the presence of hydroxyl groups on the conductive O-CNTs scaffold. Finally, the triangle in Fig. 8e corresponds to the DMPO-degradation ($A_N = 15.3$). Based on the above results and discussion, a plausible pathway active in the photoelectrochemical filtration system was proposed and displayed in Fig. 9. When the CM(50:3) photoanode was excited by the incident light, electrons and holes will be generated in the conduction bands and the valence bands of the filter, respectively. Thanks to the applied electric field, the effective charge separation ensured a rapid transport of electrons to the cathode through the external circuit. The photo-generated holes ($E_{VB} = 2.43$ V vs NHE) can react with water molecules

to produce $\cdot OH$, both contributed to the transformation of Sb(III) to Sb(V). The produced Sb(V) can be effectively sequestered by the loaded MIL-88B(Fe) due to the strong coordination between Fe₃-μ₃-oxo of CM(50:3) and Sb(V). The mass transport of the negatively-charged Sb(V) towards the positively-charged CM(50:3) photoanode filter surface could be further accelerated by the electric field due to electrostatic attraction.

3.4. Impact of solution chemistry

The effect of solution pH on the Sb(III) removal performance using the photoelectrochemical filter was examined. As suggested from Fig. 10a, the photoelectroactive filter worked steadily across a wide pH range and the optimal removal capacity for both Sb(III) and Sb_{total} was obtained at pH of 5.5. A decrease in the removal percentage was observed at higher pH values. This can be due to the different interfacial interactions between the existing Sb species and the CM(50:3) hybrid filter surface. The point of zero charge (PZC) of CM(50:3) was measured to be 7.4 (Fig. S4, Supporting Information), and aqueous Sb(III) predominantly existed as Sb(OH)₃ (pH = 3–9) and SbO₂[−] (pH > 9) (Qi et al., 2017). In addition, the preferred form of Sb(V) was Sb(OH)₆[−] from pH 3 to 11 (Rangwani et al., 2018). At pH 9.5, the surface of CM(50:3) filter also became negatively charged, leading to an electrostatic repulsion to the negatively-charged Sb(III) and Sb(V).

Additionally, experiments were carried out to examine the potential of CM(50:3) for Sb(III) purification in the presence of other conventional competitive anions (sulphate, chloride, carbonate, and phosphate) at different concentrations. When the concentration of electrolyte sulphate ranges from 0 to 5 mM, the removal efficiency of Sb_{total} increased from $56.9 \pm 1.2\%$ – $94.7 \pm 2.3\%$. However, as the sulphate concentration further increased to 10 mM, the Sb_{total} removal efficiency remained essentially unchanged. The removal percentage was constant with the concentration of chloride in the concentration range 0–10 mM. The removal efficiency of Sb_{total} decreased from $91.4 \pm 2.8\%$ – $75.3 \pm 2.3\%$ as the concentration of phosphate increased from 0 to 10 mM, this phenomenon being ascribable to the increase of pH value (8.9) caused by the hydrolysis of 10 mM carbonate. This tendency was also consistent with the results shown as a function of pH. There is a significant depression (from $90.9 \pm 3.0\%$ – $73.8 \pm 3.2\%$) in the Sb uptake when the phosphate concentration increased from 0 to 10 mM, which can be ascribed to the chemical similarity between antimony and phosphate.

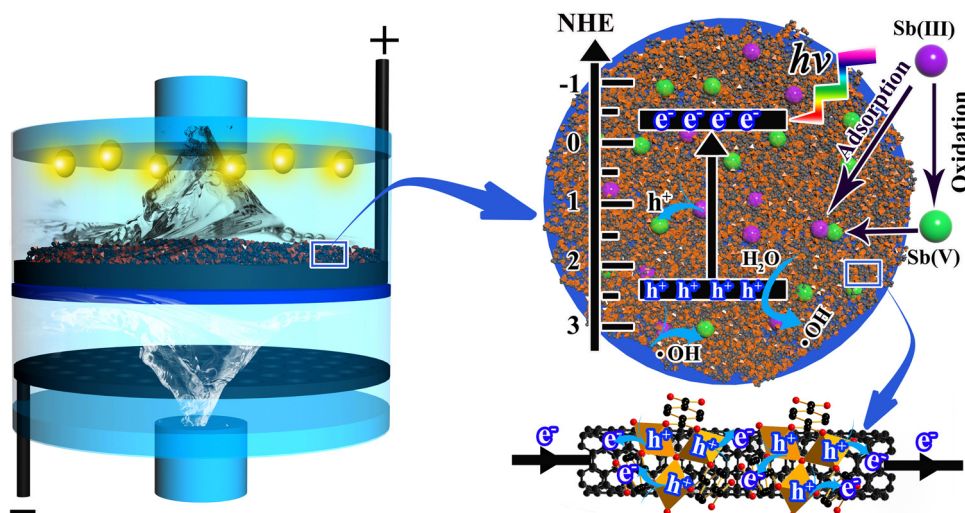


Fig. 9. Schematic illustration of the plausible photoelectrochemical decontamination mechanism of Sb(III).

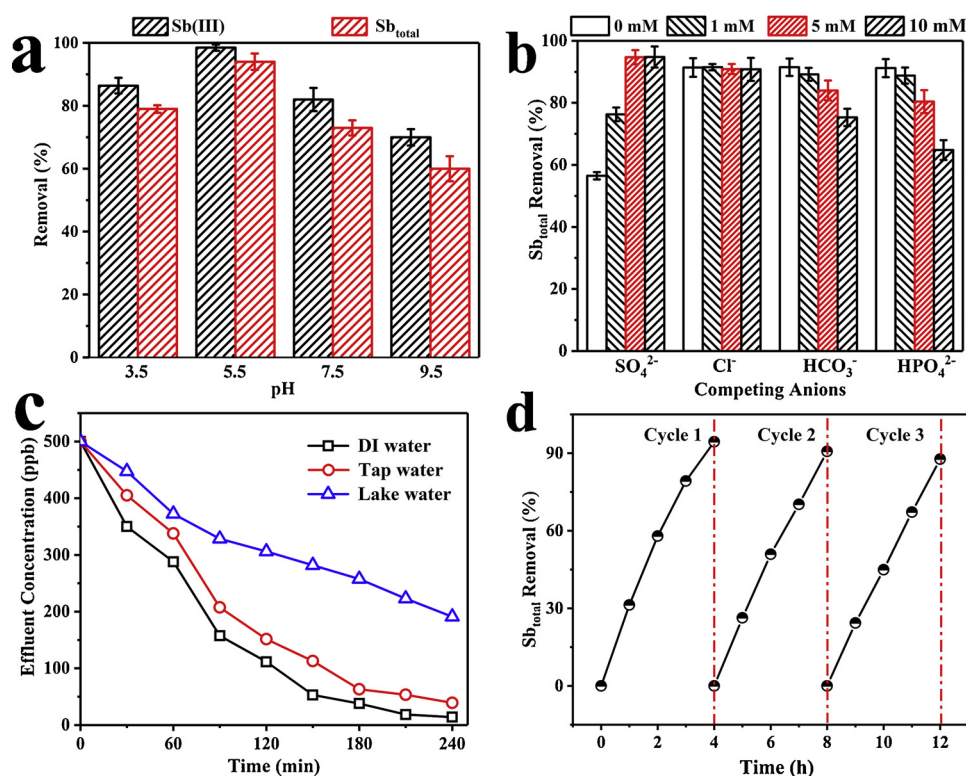


Fig. 10. Impact of (a) solution pH and (b) various competitive anions on the Sb(III) removal performance. Error bars reflect standard deviation determined by 5 times experiments. (c) Time-evolution of effluent concentration in DI water, tap water and lake water matrixes. (d) Recycle performance of the Sb(III) removal over the CM(50:3) filter. Experimental conditions: [Sb(III)]₀ of 500 ppb, flow rate of 0.5 mL/min, applied voltage of 1.5 V, [Na₂SO₄] of 5 mM, vis-light irradiation and recirculation mode.

3.5. Sb removal performance in environmental matrixes

Tap water and lake water conditions were introduced to validate the feasibility of CM(50:3) for Sb(III) purification in practical environments (Fig. 10c). The effluent concentration of Sb_{total} decreased from 500 ppb to 28 ppb after 4 h operating in tap water, similar to the performance under DI water condition, indicating that the designed system has good universality. Since lake water (total organic carbon (TOC) = 23 ± 1.9 mg/L) has a much more complicated nature than tap water (TOC concentration of 2.0 ± 0.4 mg/L), under the same experimental parameters (0.5 mL/min, vis-light + 1.5 V), the removal efficiency was only about 61.6 % after 4 h. This might be explained through the following reasons: firstly, natural organic substances in lake water would absorb on the surface of CM(50:3) and reduce the numbers of exposed active sites. Secondly, the lake water has relatively low conductivity (648 vs. 2100 μ S/cm) which would reduce the electric field and weaken the Sb(III) oxidation.

3.6. Stability evaluation

Heterogeneous advanced oxidation processes typically require robust catalysts for practical engineering applications. Hence, the stability and reusability of the flow-through system was evaluated in consecutive cycles for Sb(III) removal (Fig. 10d). Exhausted CM(50:3) filter was regenerated by passing through 100 mL of 5 mM HCl solution (Cai et al., 2016). Results suggested only marginal declined in Sb_{total} removal efficiency in three consecutive cycles, indicating the excellent stability of the photoelectrochemical filters. A series of characterizations of the used filters after three consecutive cycles also suggest similar crystal phase and iron compositions when compared with fresh CM(50:3) filter (Fig. S9, Supporting Information). Further, we determined the iron concentrations in the effluent using ICP-MS. Results indicated that only 4.5 ppb Fe was detected in the effluent over 12 h continuous filtration, accounts for only 0.74 % of the initial Fe loading.

4. Conclusions

In summary, a dual-functional photoelectrochemical filter system was rationally designed for the simultaneous oxidation and sequestration of highly toxic Sb(III). To do this, we developed a facile solvothermal route to fabricate nanoscale MIL-88B(Fe) functionalized CNT filter. The as-prepared hybrid filters are photo-responsive, highly electrically conductive, regenerable, possess regular porous network as well as sufficient exposed active sites. Upon application of vis-LED illumination and an external electric field, *in situ* conversion of Sb(III) to less toxic Sb(V) can be readily achieved. These Sb(V) compounds can be effectively further sequestered by MIL-88B(Fe). Various advanced characterization techniques were employed to provide solid evidences on the Sb(III) conversion and sequestration. The proposed technology works effectively across a wide range of solution chemistry conditions. Overall, the outcomes of this study are dedicated to provide a flow-through strategy by integrating photoelectrochemical and nanotechnology for the decontamination of Sb(III) and other similar heavy metal ions from water bodies.

CRediT authorship contribution statement

Mohua Li: Data curation, Writing - original draft. **Yanbiao Liu:** Conceptualization, Supervision, Funding acquisition. **Chensi Shen:** Investigation, Methodology. **Fang Li:** Validation, Resources. **Chong-Chen Wang:** Formal analysis, Methodology. **Manhong Huang:** Supervision. **Bo Yang:** Resources. **Zhiwei Wang:** Formal analysis. **Jianmao Yang:** Formal analysis. **Wolfgang Sand:** Writing - review & editing.

Declaration of Competing Interest

The authors declare that they have no known competing financial interests or personal relationships that could have appeared to influence the work reported in this paper.

Acknowledgements

This work was supported by the National Key Research and Development Program of China (No. 2018YFF0215703), the Fundamental Research Funds for the Central Universities (No. 2232019G-11), the Natural Science Foundation of Shanghai, China (No. 18ZR1401000), and the Shanghai Pujiang Program (No. 18PJ1400400).

Appendix A. Supplementary data

Supplementary material related to this article can be found, in the online version, at doi:<https://doi.org/10.1016/j.jhazmat.2019.121840>.

References

- Antonellini, M., Mollema, P.N., Del Sole, L., 2017. Application of analytical diffusion models to outcrop observations: implications for mass transport by fluid flow through fractures. *Water Resour. Res.* 53, 5545–5566.
- Buettner, G.R., 1987. Spin trapping-electron-spin-resonance parameters of spin adducts. *Free Rad. Biol. Med.* 3, 259–303.
- Buruga, K., Song, H., Shang, J., Bolan, N., Kalathi, J.T., Kim, K.-H., 2019. A review on functional polymer-clay based nanocomposite membranes for treatment of water. *J. Hazard. Mater.* 379.
- Cai, J., Wang, X., Zhou, Y., Jiang, L., Wang, C., 2016. Selective adsorption of arsenate and the reversible structure transformation of the mesoporous metal-organic framework MIL-100(Fe). *Phys. Chem. Chem. Phys.* 18, 10864–10867.
- Cong, Y., Ji, Y., Ge, Y., Jin, H., Zhang, Y., Wang, Q., 2017. Fabrication of 3D Bi₂O₃-BiOI heterojunction by a simple dipping method: highly enhanced visible-light photoelectrocatalytic activity. *Chem. Eng. J.* 307, 572–582.
- Dalle, K.E., Waman, J., Leung, J.J., Reuillard, B., Karmel, I.S., Reisner, E., 2019. Electro- and solar-driven fuel synthesis with first row transition metal complexes. *Chem. Rev.* 119, 2752–2875.
- Dao, X.Y., Guo, J.H., Wei, Y.P., Guo, F., Liu, Y., Sun, W.Y., 2019. Solvent-free photo-reduction of CO₂ to CO catalyzed by Fe-MOFs with superior selectivity. *Inorg. Chem.* 58, 8517–8524.
- Das, R., Vecitis, C.D., Schulze, A., Cao, B., Ismail, A.F., Lu, X., Chen, J., Ramakrishna, S., 2017. Recent advances in nanomaterials for water protection and monitoring. *Chem. Soc. Rev.* 46, 6946–7020.
- Du, X., Yi, X., Wang, P., Deng, J., Wang, C., 2019a. Enhanced photocatalytic Cr(VI) reduction and diclofenac sodium degradation under simulated sunlight irradiation over MIL-100(Fe)/g-C₃N₄ heterojunctions. *Chin. J. Catal.* 40, 70–79.
- Du, X.D., Yi, X.H., Wang, P., Zheng, W., Deng, J., Wang, C.C., 2019b. Robust photocatalytic reduction of Cr(VI) on UiO-66-NH₂(Zr/Hf) metal-organic framework membrane under sunlight irradiation. *Chem. Eng. J.* 356, 393–399.
- Duan, D., Si, X., Ding, Y., Li, L., Ma, G., Zhang, L., Jian, B., 2019. A novel molecularly imprinted electrochemical sensor based on double sensitization by MOF/CNTs and Prussian blue for detection of 17 beta-estradiol. *Bioelectrochemistry* 129, 211–217.
- Filella, M., Belzile, N., Chen, Y.W., 2012. Human exposure to antimony. II. Contents in some human tissues often used in biomonitoring (hair, nails, teeth). *Crit. Rev. Environ. Sci. Technol.* 42, 1058–1115.
- Gao, G., Vecitis, C.D., 2011. Electrochemical carbon nanotube filter oxidative performance as a function of surface chemistry. *Environ. Sci. Technol.* 45, 9726–9734.
- Guo, X., Wu, Z., He, M., Meng, X., Jin, X., Qiu, N., Zhang, J., 2014. Adsorption of antimony onto iron oxyhydroxides: adsorption behavior and surface structure. *J. Hazard. Mater.* 276, 339–345.
- Guo, W., Fu, Z., Wang, H., Liu, S., Wu, F., Giesy, J.P., 2018a. Removal of antimonate (Sb(V)) and antimonite (Sb(III)) from aqueous solutions by coagulation-flocculation-sedimentation (CFS): dependence on influencing factors and insights into removal mechanisms. *Sci. Total Environ.* 644, 1277–1285.
- Guo, C., Ran, J., Vasileff, A., Qiao, S., 2018b. Rational design of electrocatalysts and photo(electro)catalysts for nitrogen reduction to ammonia (NH₃) under ambient conditions. *Environ. Eng. Sci.* 11, 45–56.
- He, X., Min, X., Luo, X., 2017. Efficient removal of antimony (III, V) from contaminated water by amino modification of a zirconium metal-organic framework with mechanism study. *J. Chem. Eng. Data* 62, 1519–1529.
- Horcajada, P., Salles, F., Wuttke, S., Devic, T., Heurtaux, D., Maurin, G., Vimont, A., Daturi, M., David, O., Magnier, E., Stock, N., Filinchuk, Y., Popov, D., Riekel, C., Ferey, G., Serre, C., 2011. How linker's modification controls swelling properties of highly flexible iron(III) dicarboxylates MIL-88. *J. Am. Chem. Soc.* 133, 17839–17847.
- Jana, Y.M., Halder, P., Biswas, A.A., Roychowdhury, A., Das, D., Dey, S., Kumar, S., 2016. Synthesis, X-ray rietveld analysis, infrared and mossbauer spectroscopy of R₂FeSbO₇ (R³⁺ = Y, Dy, Gd, Bi) pyrochlore solid solution. *J. Alloys Compd.* 656, 226–236.
- Jian, M., Wang, H., Liu, R., Qu, J., Wang, H., Zhang, X., 2016. Self-assembled one-dimensional MnO₂@zeolitic imidazolate framework-8 nanostructures for highly efficient arsenite removal. *Environ. Sci. Nano* 3, 1186–1194.
- Kong, L., He, M., 2016. Mechanisms of Sb(III) photooxidation by the excitation of organic Fe(III) complexes. *Environ. Sci. Technol.* 50, 6974–6982.
- Kong, L., Hu, X., He, M., 2015. Mechanisms of Sb(III) oxidation by pyrite-induced hydroxyl radicals and hydrogen peroxide. *Environ. Sci. Technol.* 49, 3499–3505.
- Lei, Z.D., Xue, Y.C., Chen, W.Q., Li, L., Qiu, W.H., Zhang, Y., Tang, L., 2018. The Influence of carbon nitride nanosheets doping on the crystalline formation of MIL-88B(Fe) and the photocatalytic activities. *Small* 14, e1802045.
- Li, J., Zhang, Y., Zheng, S., Liu, F., Wang, G., 2019. Anaerobic bacterial immobilization and removal of toxic Sb(III) coupled with Fe(II)/Sb(III) oxidation and denitrification. *Front. Microbiol.* 10, 360.
- Li, J., Li, X., Hayat, T., Alsaedi, A., Chen, C., 2017. Screening of zirconium-based metal-organic frameworks for efficient simultaneous removal of antimonite (Sb(III)) and antimonate (Sb(V)) from aqueous solution. *ACS Sustain. Chem. Eng.* 5, 11496–11503.
- Lin, R., Li, S., Wang, J., Xu, J., Xu, C., Wang, J., Li, C., Li, Z., 2018. Facile generation of carbon quantum dots in MIL-53(Fe) particles as localized electron acceptors for enhancing their photocatalytic Cr(VI) reduction. *Inorg. Chem. Front.* 5, 3170–3177.
- Liu, X., Jiang, B., Yin, X., Ma, H., Hsiao, B.S., 2020. Highly permeable nanofibrous composite microfiltration membranes for removal of nanoparticles and heavy metal ions. *Sep. Purif. Technol.* 233.
- Liu, H., Zuo, K., Vecitis, C.D., 2014. Titanium dioxide-coated carbon nanotube network filter for rapid and effective arsenic sorption. *Environ. Sci. Technol.* 48, 13871–13879.
- Liu, Y., Wu, P., Liu, F., Li, F., An, X., Liu, J., Wang, Z., Shen, C., Sand, W., 2019. Electroactive modified carbon nanotube filter for simultaneous detoxification and sequestration of Sb(III). *Environ. Sci. Technol.* 53, 1527–1535.
- Majumder, M., Chopra, N., Hinds, B.J., 2011. Mass transport through carbon nanotube membranes in three different regimes: ionic diffusion and gas and liquid flow. *ACS Nano* 5, 3867–3877.
- McComb, K.A., Craw, D., McQuillan, A.J., 2007. ATR-IR spectroscopic study of antimonate adsorption to iron oxide. *Langmuir* 23, 12125–12130.
- McKinlay, A.C., Eubank, J.F., Wuttke, S., Xiao, B., Wheadey, P.S., Bazin, P., Lavalley, J.C., Daturi, M., Vimont, A., De Weireld, G., Horcajada, P., Serre, C., Morris, R.E., 2013. Nitric oxide adsorption and delivery in flexible MIL-88(Fe) metal-organic frameworks. *Chem. Mater.* 25, 1592–1599.
- Nguyen Tien, T., Ki, J., Othman, M.R., 2020. Microporous ZIF-8 and ZIF-67 membranes grown on mesoporous alumina substrate for selective propylene transport. *Sep. Purif. Technol.* 233.
- Qi, Z., Joshi, I.P., Liu, R., Li, Y., Liu, H., Qu, J., 2018. Adsorption combined with superconducting high gradient magnetic separation technique used for removal of arsenic and antimony. *J. Hazard. Mater.* 343, 36–48.
- Qi, P., Luo, R., Pichler, T., Zeng, J., Wang, Y., Fan, Y., Sui, K., 2019. Development of a magnetic core-shell Fe₃O₄@TA@UiO-66 microsphere for removal of arsenic(III) and antimony(III) from aqueous solution. *J. Hazard. Mater.* 378, 120721.
- Qi, Z., Joshi, T.P., Liu, R., Liu, H., Qu, J., 2017. Synthesis of Ce(III)-doped Fe₃O₄ magnetic particles for efficient removal of antimony from aqueous solution. *J. Hazard. Mater.* 329, 193–204.
- Rangwani, S., Howarth, A.J., DeStefano, M.R., Malliakas, C.D., Platero-Prats, A.E., Chapman, K.W., Farha, O.K., 2018. Adsorptive removal of Sb(V) from water using a mesoporous Zr-based metal-organic framework. *Polyhedron* 151, 338–343.
- Saleh, T.A., Sari, A., Tuzen, M., 2017. Effective adsorption of antimony (III) from aqueous solutions by polyamide-graphene composite as a novel adsorbent. *Chem. Eng. J.* 307, 230–238.
- Trickett, C.A., Helal, A., Al-Maythaly, B.A., Yamani, Z.H., Cordova, K.E., Yaghi, O.M., 2017. The chemistry of metal-organic frameworks for CO₂ capture, regeneration and conversion. *Nat. Rev. Mater.* 2.
- Ungureanu, G., Santos, S., Boaventura, R., Botelho, C., 2015. Arsenic and antimony in water and wastewater: Overview of removal techniques with special reference to latest advances in adsorption. *J. Environ. Manage.* 151, 326–342.
- Wang, C., Li, J., Lv, X., Zhang, Y., Guo, G., 2014. Photocatalytic organic pollutants degradation in metal-organic frameworks. *Environ. Eng. Sci.* 7, 2831–2867.
- Wu, T.L., Sun, Q., Fang, G.D., Cui, P.X., Liu, C., Alves, M.E., Qin, W.X., Zhou, D.M., Shi, Z.Q., Wang, Y.J., 2019. Unraveling the effects of gallic acid on Sb(III) adsorption and oxidation on goethite. *Chem. Eng. J.* 369, 414–421.
- Xie, D., Ma, Y., Gu, Y., Zhou, H., Zhang, H., Wang, G., Zhang, Y., Zhao, H., 2017. Bifunctional NH₂-MIL-88(Fe) metal-organic framework nanooctahedra for highly sensitive detection and efficient removal of arsenate in aqueous media. *J. Mater. Chem. A* 5, 23794–23804.
- Xu, Y., Liu, J., Xie, M., Jing, L., Xu, H., She, X., Li, H., Xie, J., 2019. Construction of novel CNT/LaVO₄ nanostructures for efficient antibiotic photodegradation. *Chem. Eng. J.* 357, 487–497.
- Yu, D., Wu, M., Hu, Q., Wang, L., Lv, C., Zhang, L., 2019. Iron-based metal-organic frameworks as novel platforms for catalytic ozonation of organic pollutant: efficiency and mechanism. *J. Hazard. Mater.* 367, 456–464.
- Zhang, Y., Li, J., Bai, J., Li, L., Chen, S., Zhou, T., Wang, J., Xia, L., Xu, Q., Zhou, B., 2019. Extremely efficient decomposition of ammonia N to N₂ using ClO[•] from reactions of HO[•] and HOCl generated in situ on a novel bifacial photoelectroanode. *Environ. Sci. Technol.* 53, 6945–6953.
- Zhao, T., Tang, Z., Zhao, X., Zhang, H., Wang, J., Wu, F., Giesy, J.P., Shi, J., 2019. Efficient removal of both antimonite (Sb(III)) and antimonate (Sb(V)) from environmental water using titanate nanotubes and nanoparticles. *Environ. Sci. Nano* 6, 834–850.
- Zhou, W., Du, G., Hu, P., Yin, Y., Li, J., Yu, J., Wang, G., Wang, J., Liu, H., Wang, J., Zhang, H., 2011. Nanopaper based on Ag/TiO₂ nanobelts heterostructure for continuous-flow photocatalytic treatment of liquid and gas phase pollutants. *J. Hazard. Mater.* 197, 19–25.
- Zhu, B.J., Yu, X.Y., Jia, Y., Peng, F.M., Sun, B., Zhang, M.Y., Luo, T., Liu, J.H., Huang, X.J., 2012. Iron and 1,3,5-benzenetricarboxylic metal-organic coordination polymers prepared by solvothermal method and their application in efficient As(V) removal from aqueous solutions. *J. Phys. Chem. C* 116, 8601–8607.
- Zhu, M., Zhai, C., Sun, M., Hu, Y., Yan, B., Du, Y., 2017. Ultrathin graphitic C₃N₄ nanosheet as a promising visible-light-activated support for boosting photoelectrocatalytic methanol oxidation. *Appl. Catal. B* 203, 108–115.